Non-commutative Tomography : applications to data analysis

Françoise Briolle, Xavier Leoncini

Abstract In this chapter, we briefly recall the theory of non-commutative tomography in a pedagogical way. We then consider its applications to signal analysis. The advantages and drawbacks of these techniques to finite samples of data are discussed. Then the method is applied, first to signals originating from reflectometry measurements in magnetized fusion plasmas, and then to data obtained from the advection of tracers in a two-dimensional time dependent flow generated by three point vortices. In the first case, we show that the tomogram allows to pick a base to represent our signal which has the advantage of isolating the reflection coming from the plasma and then to improve the estimation of the density profile. In the second case, we show how, with a "tricky transformation" the method allows us to detect Lévy flights and extract some of their properties.

1 Introduction

The notion of time has been throughout the ages of constant debate and reflexion. In physics the emergence of the theory of relativity and its consequences have related in an intertwined maner the notions of space and time, leading for instance to the definition of the meter through the speed of light since 1983. From another perspective, the classical mechanical time which is essential to Newton's second law and lead to the rise of the dynamical systems branch of physics and mathematics can be as well challenged, essentially by data analysis. Indeed physics is grounded on experi-

Françoise Briolle
CReA, BA 701, 13300 Salon de Provence, France & Aix-Marseille Université, CNRS, Centre de Physique Théorique, Campus de Luminy, Case 907 - 13288 Marseille cedex 9, France e-mail: Francoise.Briolle@cpt.univ-mrs.fr

Xavier Leoncini
Aix-Marseille Université, CNRS, Centre de Physique Théorique, Campus de Luminy, Case 907 - 13288 Marseille cedex 9, France, e-mail: Xavier.Leoncini@cpt.univ-mrs.fr

mental relevance of its laws, in order to uncover or verify these, the experimentalist acquires data usually originating from a time dependent signal. When dealing with time dependent systems, data acquisition and signal analysis become crucial, not only because, as quantum mechanics taught us, measuring something changes it, but also and quite often on the macroscopic scale because of imperfections, noise and possible biases. When dealing with almost periodic data, such as the one acquired by looking at our sky and planetary motion, we usually rely on Fourier series, who introduced them in 1822. It took though a long time to develop a full mathematical theory of the basis of this approach, which eventually leads to the notion of functional analysis, with its vector space, basis or generating ensembles, and scalar products useful to define a norm, projections and a distance between functions. In some way, using this approach we try to describe an unknown function (signal) with a set of functions that are well known. Fourier analysis was then able to be deployed using the integral formalism and the full Fourier transform. At the same time, the notion of wave-length and frequency could be seen as dual representation of time and space, and hence the notion of time or its representation could become fuzzier, leading to the notion of time-frequency representations. Following this trend, the switch to numerical treatment, the development of new algorithms such as the Fast Fourier Transform, especially tailored for finite sampled data, lead to the uncovering of some of the short-comings of Fourier analysis, and most notably for un-stationary signals, for which the time-frequency representations becomes crucial. This paved the way for the development of new signal processing tools such as for instance wavelet analysis. In this chapter we focus on another approach to signal analysis, it of course comes like most other approaches for the original vein of Fourier analysis, and is as well somewhat inspired from wavelet analysis. It however adds a new degree of freedom, in the sense that we use a parametric generating set, that allows us to tune this parameter to "optimize" our signal representation for certain desired tasks, such as isolating some components or signature from an un-stationary signal.

Most of signals are non-stationary with a time-dependent spectral content. Therefore an adequate joint time and frequency representation is desired for a characterization of such signals. Several types of linear transforms, as Gabor transform or wavelets transforms are widely used.

The Wigner-Ville quasi distribution is considered to be optimal in the sense that the spread in the time-frequency plane is minimal. But the Wigner-Ville distribution has in general positive and negative values and the interference terms (artifacts) may be non-zero and the interpretation of its representation could be delicate.

Tomograms transforms are recent mathematical techniques, based on group theory. Associated to a linear combination of non-commutative operators, tomograms are quadratic positive signal transforms. Then, in contrast to a time-frequency representation, the tomogram is the the exact probability distribution of the signal on the variable X, corresponding to a linear combination of the chosen operators. We may define as a component of the signal any distinct feature (ridge, peak, etc.) of the representation.

In section 2 we will give an overview of several transformations as linear transforms, quasi-distibutions and tomograms, which can be used to characterize unsta-

tionary signals. Non-commutative tomograms, elaborated with the generators of the one-dimensional conformal group will be presented, with a particular emphasis to the time-frequency tomogram. Then, two applications of this transformation will be extensively presented. In section 3, tomograms are used for the analysis of measurements of reflectometry on magnetized plasma, allowing to isolate the only reflection on the plasma, and then to estimate with accuracy the density profile. In section 4, the anomalous transport of particles in a flow generated by three points vortices will be detected and characterized. After a transformation of the arclength of chaotic trajectories as the instantaneous frequency of a signal, the time-frequency tomogram transformation is used for the detection and characterization of Lévy flights .

2 Non commutative tomograms

Several types of integral transform [1, 2] are used in signal processing and are applied in different fields as engineering, acoustic, communications, radar, medicine, etc.. We will consider here an analytic signal $f(t) = x(t) + iy(t)$, where $y(t)$ is the Hilbert transform of $x(t)$, where $x(t)$ is the real measured signal.

In addition to the traditional Fourier analysis [3] widely used, other transforms have been developed like the wavelet [4, 5, 6]. Recently the non commutative tomograms, based on the linear combination of non commutative operators, was suggested [7, 8]. We will present in this section a unified picture of different methods of signal processing using linear or bilinear transform in the Hilbert space. Mutual relations of the Wavelets, Wigner-Ville and tomographic transformations will be exhibited.

2.1 Linear transforms, quasi-distributions and tomograms

A unified framework to characterize linear transforms, quasidistributions and tomograms was developed in [8]. This is briefly summarized here.

Consider:

- a normalized analytic signal $f(t)$ as vectors $\mid f\rangle$ in a dense nuclear subspace $\mathscr{N}$ of a Hilbert space $\mathscr{H}$ with dual space $\mathscr{N}^*$ (with the canonical identification $\mathscr{N} \subset \mathscr{N}^*$)
- a family of operators $\{U(\alpha) : \alpha \in I,\ I \subset R^n\}$ defined on $\mathscr{N}^*$, satisfying the completeness conditions (which is the case when $U(\alpha)$ generates a unitary group $U(\alpha) = e^{iB(\alpha)}$).
- a reference vector $\langle h \in \mathscr{N}^*$ be a reference vector chosen in such way that the linear span of $\{U(\alpha)h| \in \mathscr{N}^* : \alpha \in I\}$ is dense in $\mathscr{N}^*$. This means that, out of the set $\{U(\alpha)h\}$, a complete set of vectors can be chosen to serve as a basis.

If $U(\alpha)$ is a unitary operator, there is a self-adjoint operator $B(\alpha)$, such that $U(\alpha) = e^{iB(\alpha)}$.

In this setting three types of integral transforms are constructed.

1. **Linear transform:** $W_f^{(h)}(\alpha) = \langle U(\alpha)h \,|f\rangle$

   - Fourier transform [3] is the representation of the analytic signal as a linear superposition of planes waves which are the eigenvectors $|\,\omega\rangle$ of the frequency operator $\hat{\omega} = -i\frac{d}{dt}$. The plane wave signals reads

     $$f_\omega(t) = \langle t \mid \omega\rangle = \frac{1}{\sqrt{2\pi}} e^{i\omega t}\,,$$

     and the Fourier transform of the analytic signal is

     $$F_f(\omega) = \langle \omega \mid f\rangle = \frac{1}{\sqrt{2\pi}} \int f(t) e^{-i\omega t} dt\,.$$

     This transformation is invertible and gives the possibility to reconstruct the signal $f(t)$ by means of the inverse Fourier transform

     $$f(t) = \langle t \mid f\rangle = \frac{1}{\sqrt{2\pi}} \int F(\omega) e^{i\omega t} d\omega\,.$$

     The main problem with the Fourier transform is that the signal $f(t)$ has a finite duration and the plane waves $f_\omega(t)$ are supposed of infinite duration. And in the case of unstationary signals, this transformation will not give any information of the spectral evolution in time. In fact, it is necessary to use a joint time-frequency description of the signal to get the evolution of the phase derivative (instantaneous frequency) as a function of time.

   - Gabor transform [9] or Short-Time Fourier transform [10, 11, 12] gives the possibility to represent the spectral evolution of the signal $f(t)$, using a window function of fixed width. The signal will be projected on "wave packets" of finite duration :

     $$h_{\tau,\omega}(t) = h(t-\tau)e^{i\omega t}\,,$$

     and the Gabor transform is

     $$G_f(\tau,\omega) = \langle h_{\tau,\omega} \mid f\rangle = \frac{1}{\sqrt{2\pi}} \int f(t) h^*(t-\tau) e^{-i\omega t} dt\,.$$

     For each τ, the window $h(t)$ will take only a portion of the signal beforehand the Fourier transform. To get a good resolution in time, the width of the window $h(t)$ should be very small, but then the resolution in frequency is degraded. And to get a good resolution in frequency, the window has to be

very large, and then the resolution in time is very bad. However, this transformation, also called the spectrogram, is widely used to represent unstationary signals.

- Wavelet transform [13, 14] is the projection of the signal $f(t)$ on a "basic wavelet" $h(t)$ translated and expanded :

$$h_{s,\tau}(t) = \frac{1}{\sqrt{s}} h(\frac{t-\tau}{s}) e^{i\omega t} ,$$

and the Wavelet transform is

$$W_f(s,\tau) = \langle h_{s,\tau} \mid f \rangle = \int f(t) h^*_{s,\tau}(t) dt .$$

To get a finite integral, the "basic wavelet" should satisfied the eligibility conditions such $\int h(t)dt = 0$ (zero mean) and $\int |H(\omega)|^2 \frac{d\omega}{\omega} = 1$. A lots of "basic wavelets" can be used as the Mexican hat wavelet

$$h(t) = (1-t^2) e^{-t^2/2} ,$$

or the Morlet wavelet

$$h(t) = \frac{1}{2\pi} e^{-t^2/2} e^{i\omega_0 t} .$$

Unlike the Short-Time Fourier transform which gives a unique resolution (in time or in frequency) for each point of the time-frequency plane, the wavelet transform will give different resolutions according to the frequency: for low frequency, the resolution will be good in frequency at the cost of a bad localization in time. On the contrary, for high frequency, the compression of the wavelet will allows to a good resolution in time to the detriment of the frequency resolution. This transformation elaborated in the years '80 by A. Grossman and J. Morley [15] is now used in many applications of signal processing.

2. **Quasidistribution transform:** $Q_f(\alpha) = \langle U(\alpha) f | f \rangle$

- Wigner-Ville transform [16, 17] is a bilinear map of the function $f(t)$

$$W(t,\omega) = \int f(t+\frac{u}{2}) f^*(t-\frac{u}{2}) e^{-i\omega u} du$$

Wigner-Ville quasidistribution provides information in the joint time-frequency domain with good energy resolution. But the oscillating cross-term makes the interpretation of this transform a difficult matter. Even if the average of the cross-terms is small, their amplitude may be greater than the signal in time-

frequency regions that carry no physical information. This is a consequence of the basic fact that the time ($\hat{t}$) and the frequency ($\hat{\omega} = i\frac{d}{dt}$) operators associated to this quasi distribution, are a pair of non-commutative operators and then precludes the existence of joint probabilities density in the time-frequency plane. Hence a joint probability density cannot be defined.
To profit from the time-frequency energy resolution of the bilinear transforms while controlling the cross-terms problem, modifications to the Wigner-Ville transform have been proposed. Transforms in the Cohen class [18, 19] make a two-dimensional filtering of the Wigner-Ville quasidistribution.

- Ambiguity function : the analytic signal $f(t)$ can also be described by a function called the ambiguity function of two variables

$$AF_f(\tau,\omega) = \int f(t+\frac{\tau}{2}) f^*(t-\frac{\tau}{2}) e^{-i\omega t} dt$$

This function is the two-dimensional Fourier transform of the Wigner-Ville quasidistribution. Thus, the ambiguity function contains the same information on a signal as the Wigner-Ville transformation $W(t,\omega)$.

3. **Quadratic signal transforms:** $M_f^{(B)}(X) = \langle f \mid \delta\left(B(\alpha) - X\right) \mid f \rangle$
Recently, a new type of strictly positive bilinear transforms has been proposed [7, 8], called *tomograms*, which is a generalization of the Radon transform [20] to noncommutative pairs of operators.
Let X take values on the spectrum of $B(\alpha)$. Considering a set of generalized eigenstates (in $\mathscr{N}^*$) of $B(\alpha)$, one obtains for the kernel

$$\langle Y \mid \delta\left(B(\alpha) - X\right) \mid Y' \rangle = \delta(Y' - X)\,\delta(Y - Y') = \langle Y \mid X \rangle \langle X \mid Y' \rangle$$

Therefore, we may identify $\delta\left(B(\alpha) - X\right)$ with the projector $\mid X \rangle\langle X \mid$

$$\delta\left(B(\alpha) - X\right) = \mid X \rangle\langle X \mid = P_X$$

From this, it follows

$$M_f^{(B)} = \langle f \mid \delta\left(B(\alpha) - X\right) \mid f \rangle = \langle f \mid X \rangle \langle X \mid f \rangle = \left|\langle X \mid f \rangle\right|^2, \qquad (1)$$

showing the positivity of the tomogram and its nature as the squared amplitude of the projection on generalized eigenvectors of $B(\alpha)$. For a normalized analytic signal $f(t)$, the tomogram is normalized

$$\int M_f^{(B)}(X)\, dX = 1\,.$$

Then, the tomogram can be interpreted as the probability distribution of the random variable X corresponding to the observable defined by the operator $B(\alpha)$ and provides a full characterization of the signal.

Let consider the operator $B(\alpha)$ as a linear combination of the operators $\mathscr{O}_1, \mathscr{O}_2$ and its eigeinvectors $\{\Psi_\alpha^X(t)\}$. The B-tomogram, which explores the signal along lines in the plane (O_1, O_2), is the projection of the analytic signal on the eigenvectors:

$$M_f^{(B)}(X) = \langle f, \Psi_\alpha^X \rangle = \int f(t)\Psi_\alpha^X(t)dt$$

Here, we consider one-dimensional conformal with its generators

$$\hat{t} \qquad \hat{\omega} = -i\frac{d}{dt} \qquad D = (\hat{t}\hat{\omega} + \hat{\omega}\hat{t}) \qquad K = i\left(\hat{t}^2\frac{d}{dt} + \hat{t}\right) .$$

One may elaborate a linear combination of those non commutative operators to construct one-dimensional tomograms.

- Time-frequency tomogram
  The operator $B_1(\alpha)$ is a linear combination of the time $\hat{t}$ and frequency $\hat{\omega}$ operators,
  $$B_1(\mu,\nu) = \mu\hat{t} + \nu\hat{\omega} .$$
  The eigenvectors $\Psi_{\mu,\nu}^X(t)$, associated to the eigenvalue X are
  $$\Psi_{\mu,\nu}^X(t) = e^{-i\left(\frac{\mu t^2}{2\nu} - \frac{tX}{\nu}\right)} ,$$
  and the time-frequency tomogram is the projection of the analytic signal on the eigenvectors
  $$M_1(\mu,\nu,X) = \frac{1}{2\pi|\nu|}\left|\int e^{i\left(\frac{\mu t^2}{2\nu} - \frac{tX}{\nu}\right)} f(t)\,dt\right|^2 . \tag{2}$$
  This tomogram is studied in more details in Sec. 2.2 and two applications using this transformation are extensively detailed in Sec.3 and Sec.4 .

- Time-scale tomogram
  For this tomogram, the operator $B_2(\alpha)$ is a linear combination of the time $\hat{t}$ and the dilatation operator $D = (\hat{t}\hat{\omega} + \hat{\omega}\hat{t}) = -i\left(\hat{t}\frac{d}{dt} + \frac{1}{2}\right)$, instead of the operator $\hat{\omega}$ used for the previous operator,
  $$B_2(\mu,\nu) = \mu\hat{t} + \nu D .$$
  The time-scale tomogram is defined as the projection of the signal on the eigenvectors of the operator $B_2(\mu,\nu)$ associated to the eigenvalue X,
  $$M_2(\mu,\nu,X) = \frac{1}{2\pi|\nu|}\left|\int dt\,\frac{f(t)}{\sqrt{|t|}} e^{\left[i\left(\frac{\mu}{\nu}t - \frac{X}{\nu}\log|t|\right)\right]}\right|^2 . \tag{3}$$

- Frequency-scale tomogram

This tomogram is elaborated with the operator $B_3(\alpha)$, a linear combination of the frequency operator $\hat{\omega}$ and the dilatation operator D,

$$B_3(\mu,\nu) = \mu\hat{\omega} + \nu D\,. \tag{4}$$

and then, the projections of the signal on the eigenvectors will give the frequency-scale tomogram

$$M_3(\mu,\nu,X) = \frac{1}{2\pi|\nu|}\left|\int \frac{F_f(\omega)}{\sqrt{|\omega|}} e^{\left[-i\left(\frac{\mu}{\nu}\omega - \frac{X}{\nu}\log|\omega|\right)\right]} d\omega\right|^2, \tag{5}$$

with $F_f(\omega)$ being the Fourier transform of the analytic signal $f(t)$.

- Time-conformal tomogram
  For this tomogram, the operator $B_4(\mu,\nu)$ is a linear combination of the time $\hat{t}$ and the conformal operator K

$$B_4(\mu,\nu) = \mu\hat{t} + \nu K = \mu\hat{t} + i\nu\left(t^2\frac{d}{dt} + t\right).$$

  Then, the tomograms related to this operator is

$$M_4(\mu,\nu,X) = \frac{1}{2\pi|\nu|}\left|\int dt\, \frac{f(t)}{|t|} e^{\left[i\left(\frac{X}{\nu t} + \frac{\mu}{\nu}\log|t|\right)\right]}\right|^2. \tag{6}$$

  For more details on noncommutative tomograms defined on the one-dimensional conformal group, see [21, 8].

4. **Quantum mechanics formalism**
   The linear and the quasidistribution transforms can be written using group theory formalism.
   If $U(\alpha)$ are unitary operators, by Stone's theorem, there are self-adjoint operators $B(\alpha)$ such that $U(\alpha) = e^{iB(\alpha)}$. The linear and quasidistribution transforms can be written as

$$W_f^{(h)}(\alpha) = \langle h|e^{iB(\alpha)}|f\rangle$$

$$Q_f^{(B)}(\alpha) = \langle f|e^{iB(\alpha)}|f\rangle$$

   For $B(\alpha) = \alpha_1\hat{t} + \alpha_2\hat{\omega}$ and h a generalized eigenvector of the time-translation operator, the linear transform $W_f^{(h)}$ becomes the Fourier transform. For $B(\alpha)$ plus the parity operator $\frac{\pi(\hat{t}^2+\hat{\omega}^2-1}{2}$, the $Q_f(\alpha)$ would be the Wigner -Ville transform.

Similarly, for $B(\alpha) = \alpha_1 D + \alpha_2 \hat{\omega}$ where D is the dilatation operator $D = \frac{1}{2}(\hat{t}\hat{\omega} + \hat{\omega}\hat{t})$, the linear transform $W_f^{(h)}$ is a wavelet transform and the $Q_f(\alpha)$ the Bertrand transform.

The relations between the transformations are established in [8].

2.2 Time-frequency tomogram

For an analytic signal $f(t)$, the time-frequency tomogram is defined as :

$$M_f(X,\mu,\nu) = \frac{1}{2\pi|\nu|}\left|\int f(t)\exp\left(\frac{i\mu}{2\nu}t^2 - \frac{iX}{\nu}t\right)dt\right|^2 , \tag{7}$$

For each (μ,ν) pair corresponding to a linear combination of the time and frequency operators the tomogram provides a probability distribution on the variable X [see Eq. (3)]. The tomogram $M_f(X,\mu,\nu)$ is an image in the $(X,(\mu,\nu))$ hyper-plane of the probability flow from the t-description of the signal to the frequency-description, through all the intermediate steps of the linear combination.

For an easy interpretation of the time-frequency tomogram, we consider a particular case $\mu = \cos\theta, \nu = \sin\theta$ with the self-adjoint operator $B(\theta) = \cos\theta\hat{t} + \sin\theta\hat{\omega}$. The tomogram is defined as :

$$M_f(X,\theta) = \frac{1}{2\pi|\sin\theta|}\left|\int f(t)\exp\left(\frac{i\cos\theta}{2\sin\theta}t^2 - \frac{iX}{\sin\theta}t\right)dt\right|^2 . \tag{8}$$

Then, in the plane (X,θ) the tomogram $M_f(X,\theta)$ can be interpreted as the probability distribution on the variable X. For this particular case, the tomogram $M_f(X,\theta)$ coincides with the Radon transform [22], which has already been used for signal analysis by several authors [23, 24, 25] in a different context.

For $\theta = \frac{\pi}{2}$, the tomogram $M_f(X,\frac{\pi}{2})$ is the frequency-description of the signal,

$$M_f(X,\frac{\pi}{2}) = \frac{1}{2\pi}\left|\int f(t)e^{-iXt}\,dt\right|^2 .$$

For $\theta = 0$, the operator $B(\theta) = \hat{t}$ and the tomogram $M_f(X,0)$ is the time-description of the signal. The limit of the Fresnel tomogram $M_f^F(X,\theta)$ defined for small θ in [26], is

$$\lim_{\theta\to 0} M_f^F(X,\theta) = |s(t)|^2 .$$

The variable X is the time for $\theta = 0$, the frequency for $\theta = \pi/2$ and is a generalized variable X, mixture of time and frequency, for other values of θ.

We can make the link between the time-frequency tomogram $M_f(X,\theta)$ and the fractional Fourier transform [27], defined as:

$$\mathscr{F}_s(x,\theta) = C(\theta) e^{\frac{i\pi x^2}{\tan\theta}} \int s(t) exp\left(\frac{i\pi\cos\theta}{\sin\theta} t^2 - \frac{2\pi x}{\sin\theta} t\right) dt\,. \tag{9}$$

Up to a phase factor $\exp(ix^2/2\tan\theta)$ and a normalization constant $C(\theta)$, the fractional Fourier transform is similar to the time-frequency tomogram $M_f(X,\theta)$. They can be both interpreted as the projection of the analytic signal $f(t)$ on a basis of chirp signals [28]

$$\psi_{\theta,x}(t) = e^{i\left[(\pi/2\tan\theta)t^2 - (x/sin\theta)t\right]}\,.$$

2.3 Time frequency tomogram and data analysis

2.3.1 Signal of finite duration T

For a signal of duration T the time frequency tomogram, can be written as:

$$M_s(x,\theta) = \left| \int s(t) \Psi_x^{\theta,T}(t)\, dt \right|^2 = \left| < s, \Psi_x^{\theta,T} > \right|^2 , \tag{10}$$

with

$$\Psi_x^{\theta,T}(t) = \frac{1}{\sqrt{T}} \exp\left(\frac{-i\cos\theta}{2\sin\theta}\, t^2 + \frac{ix}{\sin\theta}\, t\right) . \tag{11}$$

The family $\left\{\Psi_{x_n}^{\theta,T}(t)\right\}$ is orthogonal and normalized basis : $< \Psi_{x_m}^{\theta,T}, \Psi_{x_n}^{\theta,T} >= \delta_{m,n}$ for a family of values $\{x_n = x_0 + \frac{2n\pi}{T}\sin\theta\}$, where x_0 is freely chosen (in general we take $x_0 = 0$).

The time-frequency tomogram can be written, for each angle $\theta_1, \ldots, \theta_k, \ldots, \theta_P$, as :

$$M(x_n, \theta_k) = \left| c^{\theta_k}(x_n) \right|^2 . \tag{12}$$

For a digital signal $\{s[n]\}_{n=0,\ldots,N-1}$, of length NT, $c^{\theta_k}(x_n)$ is the Fast Fourier Transform of the digital signal :

$$c^{\theta_k}(x_n) = FFT\left(s[n] \exp\left[\frac{i\cos\theta_k}{2\sin\theta_k} n^2\right]\right) . \tag{13}$$

The fast implementation of the time-frequency tomogram is of complexity $\mathscr{O}(N\log N)$, for each θ_k.

It is then possible, from the projections $c^{\theta_k}(x_n)$ to recover the original signal $s[n]$:

$$s[n] = IFFT\left(c^{\theta_k}(x_n)\right) . \exp\left[\frac{-i\cos\theta_k}{2\sin\theta_k} n^2\right] \tag{14}$$

2.3.2 Density of magnetized plasma from reflectometry measurements

Reflectometry measurements on magnetized plasma are difficult to analyze. Indeed the signal is a mixture of components such as reflections on the porthole, on the wall of the machine and, that which is of interest, the reflection on the plasma. For this application, we use the time-frequency tomogram as a kind of "chirp filter". For an angle θ_k, the probability distribution of the signal on the variable x allows to separate the three components. Then, from the tomogram projections $c^{\theta_k}(x_n)$, we will "re-synthesize" each component and their phase derivative. We are able to extract the component of interest, the reflection on the plasma, and then to extract information of the plasma density. This application is developed in section 3.

2.3.3 Detection and characterization of Lévy flights

Transport of advected passive particles in two dimensional flows with coherent structures (vortex) is anomalous when it contains Lévy flights. The arclength of the particles trajectories are characterized by a linear behavior with respect to the time (ballistic motion). The arclength of the trajectory will be transformed as the phase derivative of a new signal to emphasize the linear part of the trajectory. Then, the time-frequency tomogram will be used to detect linear chirps in a two dimensional time-frequency representation. This application is develop in section 4.

3 Measurement of the density profile of magnetized plasma

3.1 Context

The energy confinement in ITER is predicted with scaling laws extrapolated from measurements on smaller machines as Tore Supra, Jet, etc. tokamaks. When rewritten with dimensionless parameters, large uncertainties remain on some parameter dependence such as the ratio of plasma pressure to magnetic pressure. The understanding of the anomalous transport of particles in magnetized plasmas is a key issue for a fusion reactor. The large heat and particle transport is attributed to drift wave turbulence destabilized by temperature and density gradients [29].

Density measurements play an important role in the study of the anomalous transport of magnetically confined plasma for a better understanding of the turbulence. Microwave reflectometry is a radar-like technique, widely used to measure the electronic density profile in tokamak plasmas. Reflectometers have been developed along two main applications: density profile and density fluctuations measurements [30, 31].

In the years 2010, we participated in the analysis of data coming from new reflectometers on Tore Supra [32, 33]. The goal was to extract from a mixture of multi reflections (reflectometry measurements), the sole reflection on the plasma.

In this part, we will first explain the principle of reflectometry measurements in magnetized plasma, and then give some results of tomographic data analysis, and its future applications to reflectometers.

3.2 Principle of reflectometry

Derived from radar principles, reflectometry measures the amplitude and the phase variation of a microwave $E_R(t)$ reflected inside the plasma at a cut-off layer where the refractive index n becomes zero, by mixing the reflected wave with the probing wave (reference) $E_0(t)$.

For measuring the density profile, a standard method uses a frequency sweeping of the probing wave.

$$E_0(t) = cos\{\Omega(t).t)\} \qquad with \qquad \frac{\partial \Omega(t)}{\partial t} = a.t + b\,. \tag{15}$$

Then the reflected wave is equal to $E_R(t) = A(t)cos\{\Omega(t).t) + \phi(t)\}$ This signal is multiplied by a pure frequency $cos\{\Omega(t).t)\}$ and low-pass filtered afterwards in order to get, at the output of the mixer, the signal :

$$s(t) = A(t)cos\{\phi(t)\}\,. \tag{16}$$

In the mixer output, the amplitude $A(t)$ of the reflected wave $E_R(t)$ depends on the variation of the reflectivity of the cutoff layer. This is due to geometrical effects like the divergence of the microwave beam or the tilting of the cutoff layer when a large perturbation modifies the flux surfaces. The phase $\phi(t)$, that contains the most reliable information about the plasma density, is the main quantity of interest. In part 3.3, the experimental setup, which allows us to get the amplitude and the phase of the reflected wave, are exposed in details.

There is two modes of polarization of the probing wave : the ordinary polarization, where the wave polarization is in the direction of the magnetic field B of the plasma ($E \parallel B$), so called the 0–mode, and the extraordinary polarization, X-mode, where the wave polarization is orthogonal to the magnetic field ($E \perp B$). The value of the refractive index is depending on the polarization of the probing wave, as it is shown in part 3.2.1.

3.2.1 Wave propagation in a Plasma

With the hypothesis of cold (the particles are static), homogeneous (the characteristics lengths are large in comparison to the wavelength) and stationary plasma (the

evolution time is large in comparison to the wave period), it is possible to write the equation of propagation of a plane wave [34, 35, 36]. Then, the dielectic tensor is:

$$\begin{cases} \varepsilon_{xx} = \varepsilon_{yy} = 1 - \frac{\omega_{pe}^2}{\omega^2 - \omega_{ce}^2} \\ \varepsilon_{xy} = \varepsilon_{yx} = -\frac{\omega_{ce}}{\omega} \frac{\omega_{pe}^2}{\omega^2 - \omega_{ce}^2} \\ \varepsilon_{zz} = 1 - \frac{\omega_{pe}^2}{\omega^2} \\ \varepsilon_{xz} = \varepsilon_{zx} = \varepsilon_{yz} = \varepsilon_{zy} = 0 \end{cases} \tag{17}$$

Where ω is the pulsation of the probing wave, $\omega_{pe} = \sqrt{\frac{e^2 n_e}{\varepsilon_0 m_e}}$ the electronic plasma pulsation and $\omega_{ce} = eB/m_e$ the cyclotronic electronic pulsation, n_e is the electron density, e and m_e the electronic charge and mass, ε_0 the permittivity of the vacuum.

The propagation equation of a wave, perpendicular to the direction $0y$, when the magnetic field B is constant and Oz oriented, can be written as :

$$\begin{pmatrix} \varepsilon_{xx} & -i\varepsilon_{xy} & 0 \\ i\varepsilon_{xy} & \varepsilon_{xx} - N^2 & 0 \\ 0 & 0 & \varepsilon_{zz} - N^2 \end{pmatrix} \begin{pmatrix} E_x \\ E_y \\ E_z \end{pmatrix} = \mathbf{0} \tag{18}$$

With N the refractive index, $N = kc/\omega$.

- Ordinary polarization (O-mode)
  In the ordinary polarization (O-mode), the wave polarization is in the direction of the magnetic field of the plasma ($E \parallel B$) . In this case $E_x = 0$, and the propagation equation have a unique solution:

$$N_O^2 = 1 - \frac{\omega_{pe}^2}{\omega^2} . \tag{19}$$

  Then, the cutoff frequency f_O is equal to the plasma frequency $\omega_{pe}/2\pi$ and depends only on the electron density n_e.

$$f_O = \frac{1}{2\pi} \sqrt{\frac{e^2 n_e}{\varepsilon_0 m_e}} . \tag{20}$$

  The O-mode is widely used in reflectometry, but the measurements can be done only for density gradient between 0.3 and 0.8. The edge and the center density of the plasma can't be reached with this kind of measurements.
- Extraordinary polarization (X-mode)
  In the extraordinary polarization, the wave polarization is orthogonal to the magnetic field ($E \perp B$). Then, the refractive index is equal to :

$$N_X^2 = 1 - \frac{\omega_{pe}^2(1-\frac{\omega_{pe}^2}{\omega^2})}{\omega^2 - \omega_{pe}^2 - \omega_{ce}^2}\,. \tag{21}$$

If the frequency f of the probing wave is equal to $\frac{1}{2\pi}\sqrt{\omega_{pe}^2-\omega_{ce}^2}$, then the wave will become evanescent and will be absorbed by the plasma.
The wave will be reflected when $N_X = 0$. There are two cut-off frequencies, namely the upper-f_X^{up} and lower-$f_X low$:

$$f_X^{up} = \frac{1}{2\pi}\frac{\sqrt{\omega_{ce}^2+4\omega_{pe}^2}+\omega_{ce}}{2} \quad and \quad f_X^{low} = \frac{1}{2\pi}\frac{\sqrt{\omega_{ce}^2+4\omega_{pe}^2}-\omega_{ce}}{2}\,. \tag{22}$$

The edge density can be probed using the upper cutoff frequency since the frequency is finite. It allows us to measure weak density at the edge of the plasma.

3.2.2 Density profile reconstruction

Using the WKB approximation [38] along the propagation path (1D approximation), the phase variation between the antenna at $r = 0$ and the reflecting layer at $r = r_{co}$ can be estimated:

$$\phi_p = \frac{4\pi}{c}.f.\int_{r=0}^{r=r_{co}} N(r,f,t)dr - \frac{\pi}{2}\,. \tag{23}$$

Where f is the frequency of the probing wave, N(r,f,t) the plasma refractive index at the frequency f. The term $-\frac{\pi}{2}$ indicate that the reflection inside the plasma is nonmetallic.

A variation of the phase ϕ_p can be due either to a variation of the probing frequency or a variation of the optical path length between the antenna and the cut-off layer along the line of sight. Temporal changes of the phase can thus be written as:

$$\frac{\partial\phi_p}{\partial t} = \frac{4\pi}{c}.\frac{\partial f}{\partial t}.\int_{r=0}^{r=r_{co}} N(r,f,t)dr + \frac{4\pi}{c}.f.\frac{\partial}{\partial t}\left(\int_{r=0}^{r=r_{co}} N(r,f,t)dr\right)\,. \tag{24}$$

The first term is proportional to the optical path length $\int_{r=0}^{r=r_{co}} N(r,f,t)dr$, i.e. the position r_{co} of the reflecting layer, when the frequency f is swept.

The second term describes the phase changes introduced by fluctuations of the optical path length arising from temporal and spatial fluctuations of the electron density.

The beat frequency is defined as:

$$f_b = \frac{1}{2\pi}\frac{\partial\phi_p}{\partial t}\,, \tag{25}$$

and the group delay of the reflected wave, namely the time of flight :

$$\tau_g = \frac{1}{2\pi}\frac{\partial \phi_p}{\partial f} = f_b / \frac{\partial f}{\partial t}\,. \tag{26}$$

- Ordinary polarization (O-mode)
  It is possible to reconstruct a monotonic density profile, with the estimation of the group delay τ_g of the reflected wave. The localization of the reflecting layer $r_c(F_p)$ for the frequency F_p is given by the analytic expression [37]:

$$r_c(F_p) - a = \frac{c}{\pi}\int_0^{F_p} \frac{\tau_g(f)}{\sqrt{F_p^2 - f^2}} df\,. \tag{27}$$

- Extraordinary polarization (X-mode)
  In the extraordinary polarization (X-mode), the density profiles are recovered from the phase using the Bottolier algorithm [39]. Initialization of the profile is the most interesting feature of the X-mode polarization. Contrary to the O-mode polarization, where at zero density the cutoff frequency equals zero, in X mode the edge density profile position can be setup with the rise of the detected amplitude. Assuming that the first cutoff is for a null density, the start of the plasma can be set providing knowledge of the local magnetic field.

3.3 Experimental setup

A broadband reflectometer operating in the frequency range 50-75 GHz (V-Band) in extraordinary mode polarization has been developed on Tore Supra to measure edge density profiles [40, 41, 42].

Fast sweeping improves greatly the profile reconstruction. On Tore-Supra, the cut-off layer displacement during the turbulence correlation time (microsecond range) is comparable to the turbulence correlation length (centimeter range). At a sweeping rate of 1 GHz μs^{-1}, the wavelength rate is 30 cm μs^{-1}, which is comparable to the displacement of the cutoff layer. With the experimental setup described on Fig. 1, the probing wave operates in the range 50-75 GHz with a sweeping rate of 20 μs.

The output of a HTO (Hyperabrupt varactor Tuned Oscillator) providing fast linear frequency sweeps from 12-19 GHz in 20 μs, is mixed to a low frequency signal $fm \sim 100$ MHz.

After amplification, the frequency $\omega(t) + fm$ is multiplied by 4 to provide a probing signal with a frequency coverage between 48-76 GHz. The probe signal $E_0(t) = cos(4\{\omega(t) + f_m\}.t)$ is then emitted through wave guides.

Emission and reception are done with two separate identical rectangular antennas, one near of the other, outside the vacuum vessel through a porthole, around 120 cm away from the plasma edge, as it is shown in Fig. 2.

A sweep is done before every discharge and the reflection on the inner wall of the vessel is used as a reference to correct the dispersion in waveguides and antennas.

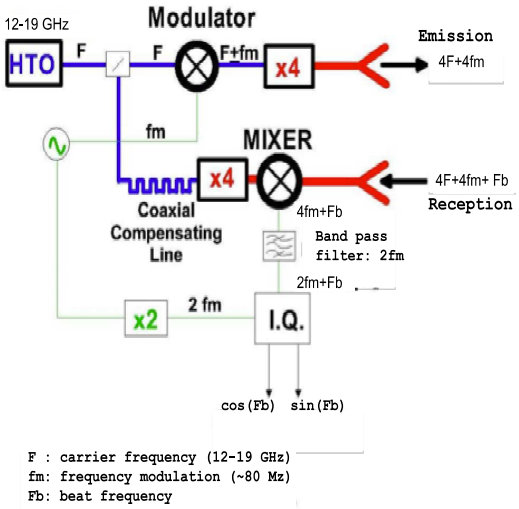

Fig. 1 X-mode Reflectometer working in V-Band (50-75 GHz)

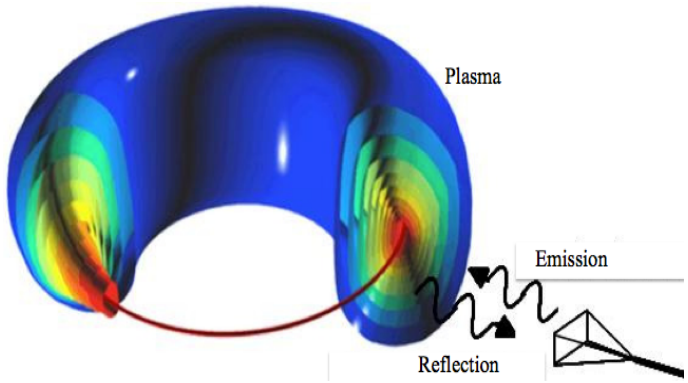

Fig. 2 The experimental setup is located outside the vacuum vessel, close to the plasma edge.

The output of the HTO, at the frequency $4\omega(t)$, is τ delayed by a delay line, to obtain the signal : $u(t) = cos(4\omega(t).(t+\tau))$. During the time τ, the path of the probing wave is equal to $D = \tau.c$, where D is the distance from the emitting antenna to the inner wall of the vessel. Then, the phase differences between the probing and the reflected waves will be mainly due to the position of the cutoff layer.

The reflected wave, $E_R(t) = A(t)cos\{(4\omega(t) + 4f_m).(t+\tau_R) + \phi(t)\}$, is then mixed to $u(t)$ and band-pass filtered at $4fm \pm 50MHz$ to obtain a low frequency signal $v(t) = A(t)cos\{(4f_m t + \phi(t)\}$.

An heterodyne demodulation at $4f_m$, providing in-phase and 90° phase detection, leaves the reflected wave in the base-band leaving only the cutoff data of the probing frequency $s(t) = A(t)e^{i\phi(t)}$.

The reflectometer can achieve a repetition rate of $5\mu s$ between sweeps, so the dynamic behavior of fast plasma events can be followed.

3.4 Data processing

The goal is to measure the density at the edge of the plasma on the extraordinary mode polarization (X mode) on Tore Supra.

The sweep-frequency reflectometer launches a probing wave in the V band (50–75 GHz). The reflectometry system repeatedly sends sweeps of duration $20\mu s$. The heterodyne reflectometers, with I/Q detection, provide a good Signal to Noise Ratio, up to 40 dB.

As it is described in detail in part 3.3, for each sweep, the reflected chirp $E_R(t)$ is mixed with the incident sweep $E_{ref}(t)$ and only the interference term is recorded as an in-phase and a 90° phase shifted sampled signals. Let the reflected signal be :

$$s(t) = x_1(t) + ix_2(t) = A(t)e^{i\varphi(t)}\,. \tag{28}$$

For one of the measurement (choc #42824) the Gabor Transform $G_s(t,\omega)$ namely the spectrogram, gives a time-frequency representation of the signal $s(t)$ [6].

$$G_s(t,\omega) = \frac{1}{\sqrt{2\pi}} \int_{-\infty}^{+\infty} s(\tau) e^{-\pi(\tau-t)^2} e^{-i\omega\tau} d\tau\,.$$

The Gabor Transform is obtained with short time Fourier transforms (STFT) of the sampled signal broken up into M windowed chunks, which usually overlap, and Fourier transformed. The spectrums are then "laid side by side" to form the image or a three-dimensional surface. For a better representation, the amplitude of the spectrum are represented by gray scales, to obtain a two dimensional image where the horizontal axis is the time and the vertical one the beat frequency. Each vertical line represent the spectrum of a trunk (Fig. 3).

The signal $s(t)$ is sampled at the frequency of 100 MHz, so we get only 2000 samples by trial. For a nice time-frequency representation, the length of the chunks is equal to 100 samples with an overlapping equal 90%.

As it can be seen on the time-frequency representation, the base-band reflected wave $s(t)$ is a mixture of different signals: a reflection of the probing wave on the inner wall of the vessel ($0 < t < 10$ μs ; beat frequency $\sim$ 20 MHz) a reflection on the porthole, placed in front of the antennas ($0 < t < 12\mu s$; beat frequency $\sim$ -5 MHz) and the reflection on the cutoff layers of the plasma ($7 < t < 20$ μs; beat frequency between 5 to 20 MHz). The reflections on the inner wall and the porthole are represented by straight lines while the plasma reflection is more heckled.

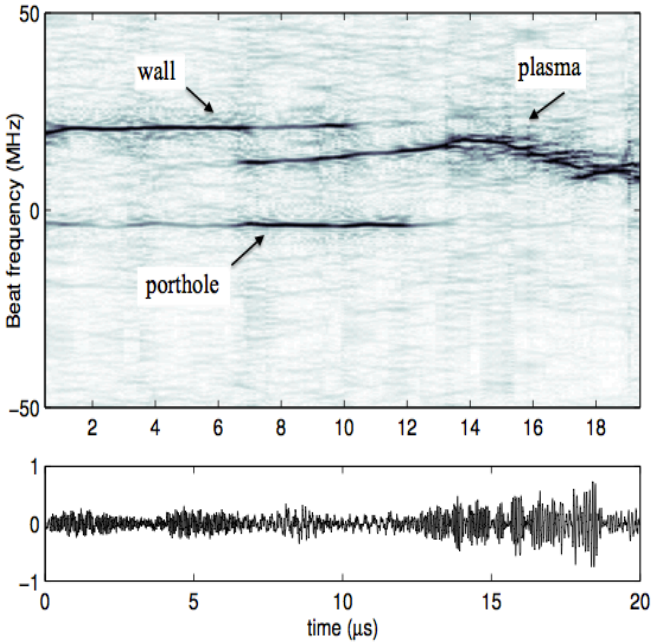

Fig. 3 *Up* Time-frequency representation of the base-band downshifted reflected wave $A(t)e^{\phi(t)}$. *Down* Real part of the base-band downshifted reflected wave.

The goal is then to extract only the reflection on the plasma from the base-band reflected wave. The reflections are overlapping in time and in frequency, the reflection on the inner wall is very close to some reflections on the plasma : a band pass filter will not give good results.

A time frequency tomographic analysis is therefore used to achieved the separation of different reflections merged in the reflected wave.

3.5 Tomographic analysis

3.5.1 Time-frequency tomograms (signal of finite duration)

In part 1, we described in much detail the time-frequency tomograms. Here, we will describe the method of component separation for the operator :

$$B_\theta^S = cos\theta\ t + sin\theta\ \omega\,, \tag{29}$$

where t and $\omega = i\frac{\partial}{\partial t}$ are respectively the time and frequency non commutative operators.

A probability family of distributions, $M_s(x,\theta)$, is defined from a complex signal $s(t)$, $t \in [0,T]$ by:

$$M_s(x,\theta) = \left| \int s(t) \Psi_x^{\theta,T}(t)\, dt \right|^2 = \left| < s, \Psi_x^{\theta,T} > \right|^2 , \tag{30}$$

with

$$\Psi_x^{\theta,T}(t) = \frac{1}{\sqrt{T}} e^{i\left(\frac{-\cos\theta}{2\sin\theta} t^2 + \frac{x}{\sin\theta} t\right)} . \tag{31}$$

Note that the $\Psi_x^{\theta,T}$ are generalized eigenfunctions for any spectral value x of the operator B_θ^S. Therefore $M_s(x,\theta)$ is a (positive) probability distribution as a function of x for each θ.

A glance at the shape of the functions (31) shows that, for fixed θ, the oscillation length at a given t decreases when $|x|$ increase. As a result, the projection of the signal on the $\left\{\Psi_{x_n}^{\theta,T}(t)\right\}$ basis locally explores different scales. On the other hand the local time scale is larger when θ also becomes larger, in agreement with the uncertainty principle for a non-commuting pair of operators.

Here θ is a parameter that interpolates between the time and the frequency operators, thus running from 0 to $\pi/2$ whereas x is allowed to be any real number. For $\theta = 0$, the tomogram $M_s(x,\theta)$ is the probability distribution of the signal in time $|s(t)|^2$ and for $\theta = \frac{\pi}{2}$, the probability distribution of the signal in frequency $|S(f)|^2$.

Our strategy is to search for intermediate values of θ where a good compromise may be found to separate the components of the signal. For such intermediate values it is possible to pull apart different components of the signal (see Fig. 4, a tomographic representation ($0 < \theta < \frac{\pi}{2}$) of the reflected wave).

As it can be seen on Fig. 5, an intermediate value of $\sin\theta \sim 0.6$ ($\theta = \frac{\pi}{5}$) allows us to separate the three components, taking into account both time and frequency information.

The Fourier transform of $s(t)$(left part Fig. 5), shows that it is impossible to use a band pass-filter to get the only reflection on the plasma. With a tomogram of the signal, for $\theta = \frac{\pi}{5}$, the three components can be distinguished (right part Fig. 5).

3.5.2 Components factorization

Method

First we select a subset of numbers $\{x_n\}$ in such a way that the corresponding family $\left\{\Psi_{x_n}^{\theta,T}(t)\right\}_n$ is orthogonal and normalized:

$$< \Psi_{x_m}^{\theta,T}, \Psi_{x_n}^{\theta,T} > = \delta_{m,n} . \tag{32}$$

This is possible using the sequence

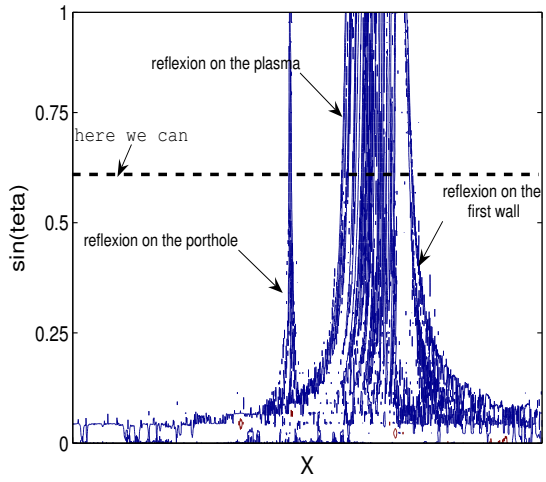

Fig. 4 Time-frequency tomographic representation of the base-band reflected wave $A(t)e^{\phi(t)}$. For $\theta = 0$, the tomogram $M_s(x,\theta)$ is probability distribution of $|s(t)|^2$ and for $\theta = \frac{\pi}{2}$, the probability distribution of $|S(f)|^2$.

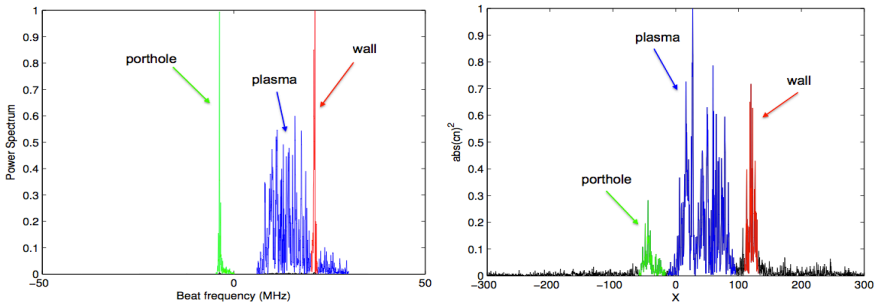

Fig. 5 *Left*: Fourier transform of the base-band signal $s(t)$ measured at the output of the reflectometer. *Right*: Tomogram, for $\theta = \frac{\pi}{5}$ of the signal $s(t)$.

$$x_n = x_0 + \frac{2n\pi}{T}\sin\theta\,, \tag{33}$$

where x_0 is freely chosen (in general we take $x_0 = 0$ but it is possible to make other choices, depending on what is more suitable for the signal under study).

We then consider the projections of the signal $s(t)$ on the orthonormal basis $\{\Psi_{x_n}^{\theta,T}\}$

$$c_{x_n,\theta}^{s} = < s, \Psi_{x_n}^{\theta,T} >\,, \tag{34}$$

and use the coefficients $c^s_{x_n,\theta}$ for our signal processing purposes.

As it is shown on the right part of the Fig. 4, it is possible, using a threshold, to select three subsets $\mathscr{F}_k$ of the $\{x_n\}$. A multi-component analysis of the signal [32] is done by reconstructing the partial signals :

$$s_k(t) = \sum_{n \in \mathscr{F}_k} c^s_{x_n,\theta} \Psi^{\theta,T}_{x_n}(t) \qquad\qquad k = 1,2,3\,. \tag{35}$$

Results

From the projections of the signal $s(t)$ on the orthonormal basis $\{\Psi^{\theta,T}_{x_n}\}$, for $\theta = \frac{\pi}{5}$, using a threshold ($\varepsilon = 0.04$) it is possible to select the spectral projections of three different components (see Fig 6).

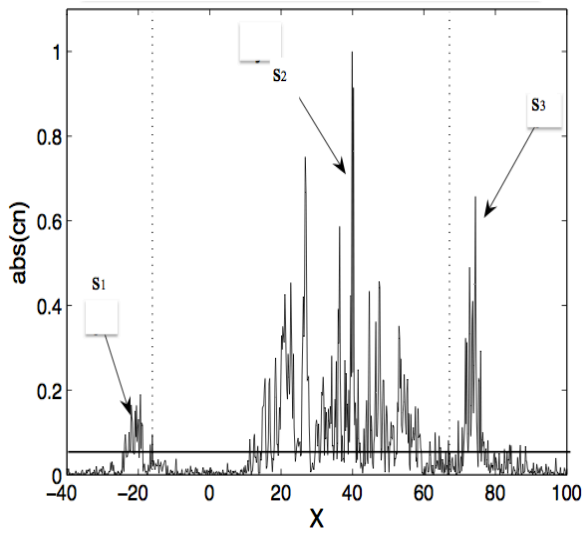

Fig. 6 Tomogram of the signal $s(t)$ for $\theta = \frac{\pi}{5}$, $M_s(x, \theta = \frac{\pi}{5})$.

First component, the reflection on the porthole

The first component, $\tilde{s_1}(t)$ corresponds to $-20 \leq x_n \leq 0$ and is therefore defined as:

$$\tilde{s_1}(t) = \sum_{x_n=-20}^{0} c^{\theta}_{x_n}(y) \Psi^{\theta}_{x_n}(t)\,. \tag{36}$$

This component is the reflection of the probing wave on the porthole. The distance from the emitting/reception antenna to the porthole is around 80 cm. It is a constant low frequency signal (see Fig 7): the phase derivative of the reflection is proportional

to the distance from the antenna to the reflector. The duration of this signal is around 12 μs.

Second component, reflection on the plasma

The second component is the reflection on the cutoff frequency of the plasma (see Fig 7). The reflection starts around 10 μs after the reflection on the porthole. The frequency and the amplitude of this reflected wave is quite heckled. This component, $\tilde{s_2}(t)$, corresponds to $0 \leq x_n \leq 110$ and is therefore defined as:

$$\tilde{s_2}(t) = \sum_{x_n=0}^{110} c_{x_n}^{\theta}(y)\Psi_{x_n}^{\theta}(t)\,. \tag{37}$$

Third component, reflection on the inner wall of the vessel

The last component corresponds to the reflection of the probing wave on the wall of the vacuum vessel. The frequency is quite constant (Fig. 7), and related to the distance antenna-wall. The duration of this signal is around 10 μs. This component, $\tilde{s_3}(t)$, corresponds to $110 \leq x_n \leq 140$ and is therefore defined as:

$$\tilde{s_3}(t) = \sum_{x_n=10}^{140} c_{x_n}^{\theta}(y)\Psi_{x_n}^{\theta}(t)\,. \tag{38}$$

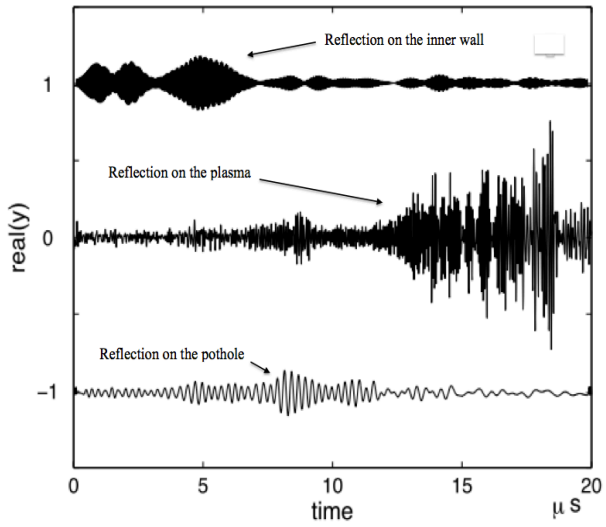

Fig. 7 The three components of the reflectometry signal. For visual purposes, the average of $\tilde{s_1}(t)$ is shifted to 1 and the average of $\tilde{s_3}(t)$ to -1.

3.5.3 Estimation of the phase derivative

Method

To compute the density profile of the plasma, with reflectometry measurements in the X-mode, it is necessary to estimate the phase derivative of the reflection on the cutoff layer of the plasma. The usual process is to isolate this refection and then, to unwrap the phase using a classical gradient procedure. Given a signal $s(t) = A(t)e^{i\phi(t)}$, the time derivative of the phase may be obtained from

$$\frac{\partial}{\partial t}\phi(t) = \mathrm{Im}\left(\frac{\frac{\partial s}{\partial t}}{s(t)}\right). \tag{39}$$

Using a tomographic decomposition allows us to get the time derivative of the phase directly. Let us remember that :

$$\tilde{s_k}(t) = A_k(t)e^{i\phi_k(t)} = \sum_{n\in\mathscr{F}_k} c^s_{x_n,\theta}\Psi^{\theta,T}_{x_n}(t) \qquad k = 1,2,3\,, \tag{40}$$

then,

$$\frac{\partial}{\partial t}\tilde{s_k}(t) = \sum_{x_n} c^s_{x_n,\theta}\frac{\partial}{\partial t}\Psi^{\theta,T}_{x_n}(t)\,. \tag{41}$$

Notice that an explicit analytic expression for $\frac{\partial}{\partial t}\Psi^{\theta,T}_{x_n}(t)$ is known, namely:

$$\frac{\partial}{\partial t}\Psi^{\theta,T}_{x_n}(t) = i\left(\frac{-\cos\theta}{\sin\theta}t + \frac{x}{\sin\theta}\right)\Psi^{\theta,T}_{x_n}(t)\,. \tag{42}$$

Therefore we obtain a direct expression for the phase derivative in terms of the coefficients $c^s_{x_n,\theta}$ without having to use the values of s_k for neighboring values of t.

$$\frac{\partial}{\partial t}\phi_k(t) = \mathrm{Im}\left(\frac{\sum_{x_n} c^s_{x_n,\theta} i\left(\frac{-\cos\theta}{\sin\theta}t + \frac{x}{\sin\theta}\right)\Psi^{\theta,T}_{x_n}(t)}{\sum_{x_n} c^s_{x_n,\theta}\Psi^{\theta,T}_{x_n}(t)}\right) \qquad k = 1,2,3\,. \tag{43}$$

This provides a more robust method to estimate the derivative. The phase derivative of the three components obtained with this method is plotted on the time-frequency representation of the signal (Fig 8).

Results

The expression of the phase derivative $\frac{\partial}{\partial t}\phi_k(t)$, given by the Eq.(43), is true for all $t \in [0,T]$.

As it can be seen on Fig. 7, the reflections on the porthole ($\tilde{s_1}$) and the inner wall ($\tilde{s_3}$) are very weak $t > 11\mu s$. The reflection on the plasma ($\tilde{s_2}$) starts only after $7\mu s$. The phase derivative will be computed only when the signal exists.

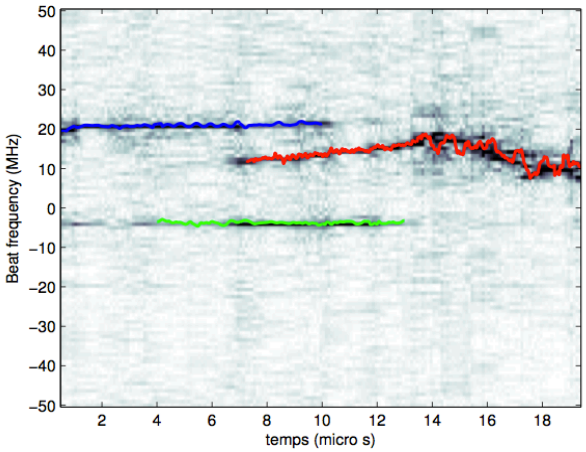

Fig. 8 The phase derivative of the three components, estimated by the tomogram method, is plotted on the time-frequency representation of the signal $s(t)$

For some values of t, the denominator in Eq.(43) could be very small, and then the estimation of the phase derivative is not good. To overcome this problem, we use a low pass filter. More details are given in [33].

The estimation of the phase derivative of the three components, with the method described above, are plotted on the time-frequency representation of the full signal $s(t)$. The method gives good results as it shown on Fig. 8.

The data processing (tomogram) will be used for the new reflectometer on Tore Supra and on Jet [43, 44, 45, 46].

4 Detection and characterization of Lévy flights

4.1 Context : Stickiness and Lévy flights in chaotic advection

In order to detect Lévy flights, we shall consider a specific physical context namely the stickiness phenomenon which leads to the presence of such flights. For this purpose we shall introduce briefly this phenomenon, in the case when it occurs in low-dimensional Hamiltonian systems[47]. To be more explicit stickiness occurs at the border between an island of regular motion and the chaotic sea. This stickiness induces naturally long correlations and as such memory effects and so-called Lévy flights. We consider a specific physical context for which this phenomenon has been explicitely exhibited. This will allow the reader to get a better intuition on physical mechanisms behind the stickiness and how it affects transport properties. The considered system is the advection of passive tracers by a two dimensional time

dependent flow leading to the phenomenon of chaotic advection. For this purpose and in order to be more explicit we shall consider a specific flow generated by three point vortices (see for instance [48]).

4.1.1 Chaotic advection

Let us start by giving some definition and clarifying the background of chaotic advection. Let us consider a flow $\mathbf{v}(\mathbf{r},t)$ of an incompressible fluid ($\nabla \cdot \mathbf{v} = 0$), and a particle advected by this flow: one can for instance picture a small object floating on the surface of a river and transported by the stream. We then need to introduce the notion of passive particle or passive tracer. This notion defines an idealized particle which presence and motion in the fluid imposes no feedback on the flow and thus does not modify it. By definition this would be true for a fluid particle itself, but for other type of particles or tracers this is usually not true. However if the size of particle is small enough with respect to the length scales involved in the system and governing the flow, and other factors such as density, rugosity etc are more or less those of the considered fluid this ideal hypothesis is a good approximation. We can then derive the equation of motion of a passive particle which transported by the fluid so that its speed equals that of the fluid and hence its motion is governed by:

$$\dot{\mathbf{r}} = \mathbf{v}(\mathbf{r},t)\,, \tag{44}$$

where $\mathbf{r} = (x,y,z)$ refers to the tracer's position, and the $\dot{}$ to the time derivative.

We shall see now how this relates to Hamiltonian chaos. In fact for an incompressible flow, we can define a stream function which resumes to a scalar field for a two dimensional system, such that the fluid velocity can be written as

$$\mathbf{v} = \nabla \wedge (\Psi \mathbf{z})\,, \tag{45}$$

where $\mathbf{z}$ corresponds to the unit vector perpendicular to the two dimensional space. Using Ψ, we can rewrite the equations governing the motion of a passive tracer Eq. (44) projected on each coordinate, as

$$\dot{x} = \frac{\partial \Psi}{\partial y}, \qquad \dot{y} = -\frac{\partial \Psi}{\partial x}\,. \tag{46}$$

And we recognize Hamilton equation of motion, where the space coordinates (x,y) are actually canonically conjugated and the stream function Ψ acts as an Hamiltonian.

When the flow is time independant, then the Hamiltonian Ψ reduces to an autonomous one degree of freedom system and is therefore integrable, which translates into the particular considered case that our passive tracers are following velocity field lines. However, it is possible and likely that the stream function Ψ is actually time-dependent. In this case, we have actually an non-autonomous system and we have a time dependent Hamiltonian system, meaning a system with $1-\frac{1}{2}$

degrees of freedom. And it is know that generically, such systems generate so-called Hamiltonian chaos. Note that this choatic phenomenon can also occur in a stationary incompressible flow, but then the flow has to be three-dimensional, and we talk about chaos of field lines, see for instance [49] and references therein.

In the context of the advection of particles in flows, this chaotic nature of trajectories was called as a phenomenon of chaotic advection [50, 51, 52]. One of the major consequence of this phenomenon concerns the mixing of trajectories. Indeed chaotic advection can enhance drastically the mixing properties of the flow, meaning that the mixing process generated by the chaotic motion is much more efficient than the one occurring through molecular diffusion. And this effect is even more patent when the flow is laminar [53, 54, 55, 56, 57]. When dealing with mixing in micro-fluid experiments and devices, chaotic advection becomes crucial. Indeed since the Reynolds number are usually small, chaotic mixing becomes, de facto, an efficient way to mix. There are also numerous domains of physics, displaying chaotic advection-like phenomena, for instance in geophysical flows or magnetized fusion plasmas [58, 59, 60, 61, 62, 63, 64, 65, 66].

To detect the Lévy flights we use data coming from the simulation of passive tracers advected by the flow generated by three point vortices. We now shall recall quickly what is a point vortex and how they appear and can be useful in two-dimensional flows.

4.1.2 Definition of a point vortex

In order to describe the notion of a point vortex it is convenient to start with Euler equation. In fact, when considering a perfect two-dimensional incompressible flow governed by the Euler equation, if we are interested in the dynamics of the vorticity field Ω, we simply take the rotational of the Euler equation. This helps getting rid of the pressure and other potential forces gradients and we end up with the following equation

$$\frac{\partial \Omega}{\partial t} + \{\Omega, \Psi\} = 0\,,\ \Omega = -\nabla^2 \Psi\,, \tag{47}$$

where $\{\cdot,\cdot\}$ corresponds to the Poisson brackets. In order for the point vortices to "appear", we assume a vorticity field given by a superposition of point concentrated vorticities (Dirac functions) written as

$$\Omega(\mathbf{r},t) = \sum_{i=1}^{N} k_i \delta\left(\mathbf{r} - \mathbf{r}_i(t)\right)\,, \tag{48}$$

where, k_i is the vorticity of a point vortex, and the vortex is localized by the point $\mathbf{r}_i(t)$ in the plane. This singular distribution is actually an exact solution of the Euler equation (47) when each of the N vortices obeys a specific and prescribed motion [67]. In fact the dynamics of the vortices ends up being equivalent to the one coming from an N-body Hamiltonian dynamics. The form of the Hamiltonian is strongly related to the Green function and therefore depends on the considered boundary

conditions. Typically if one considers no specific boundary conditions, meaning that we allow the flow to evolve on the whole plane. In this case, the Hamiltonian is quite simple and writes

$$H = \frac{1}{2\pi} \sum_{i>j} k_i k_j \ln |\mathbf{r}_i - \mathbf{r}_j| \,, \tag{49}$$

where the canonically conjugated variables are $k_i y_i$ and x_i. This is reminiscent of the passive tracer Hamiltonian as the canonical variables are intimely linked to the vortex position $\mathbf{r}_i(t)$ in the plane, however it is important to recall that the phase space corresponds now to a 2N dimensional space.

The equations of motion derived from Hamiltonian (49) juste state the fact that each vortex is advected by the velocity field generated by the other vortices. We also can note that since we know in time the positions of the point vortices, we know as well the stream function (the Hamiltonian governing passive tracers) of the flow:

$$\Psi(\mathbf{r},t) = -\frac{1}{2\pi} \sum_{i=1}^{N} k_i \ln |\mathbf{r} - \mathbf{r}_i(t)| \,. \tag{50}$$

As a last remark and important point concerning point vortex dynamics, it is important to notice that the Hamiltonian (49) is invariant by translation and by rotation. There are thus three constant of the motion besides the "energy" associated to these symmetries. However only three integrals are really in involution and Hamiltonian chaos appears in point vortex motion when we have more than $N = 3$ vortices [68, 69, 70, 71]. Note that point vortices can be also useful to model some geophysical flows [72]. And that three vortices can have singular solution, leading to finite time singularities which can lead to interesting properties and considerations [70, 73].

In order to obtain a regular (laminar) and time dependent flow, the flow generated by three vortices is a good compromise. Indeed the integrable motion of three point vortices shows a larges variety of behaviors, quasi-periodic and aperiodic flows are both possible [68, 69, 70], and are more easy to tackle than flows with more vortices see for instance [74, 71], as Poincaré maps can be computed [75, 76, 48]. In order to choose among the different possibilities, we would like to point out that usually, to address transport properties, asymptotic (large times) behavior and time translational properties are desired. So in order to achieve a situation where these features exist, we have had to consider the quasi-periodic motion of vortices. Note that these discussions are inspired by the work related to transport of passive tracers in the case of three identical vortices found in [75, 76] and the one reported in [48] corresponding to a situation of vortices with vorticities with different signs.

4.1.3 Stickiness and Anomalous transport

Until now, we have briefly reviewed the notion of chaotic mixing in a flow generated by three point vortices. As a matter of fact transport in these systems is potentially anomalous [48]. In order to emphasize what we mean by anomalous, we would like to remind the reader that the type of transport can be defined by considering the behavior of the second moment of the displacement distribution and for instance extracting a value of a characteristic exponent. If we proceed as mentionned, we end up with a rough definition of anomalous transport, meaning that transport is said to be anomalous when it is not Gaussian (diffusive), meaning that

$$\langle X^2 - \langle X \rangle^2 \rangle \sim t^{\mu}\,, \tag{51}$$

with $\mu \neq 1$ and as such:

1. If $\mu < 1$ transport is anomalous and sub-diffusion is present.
2. If $\mu = 1$ transport is Gaussian and we have diffusion.
3. If $\mu > 1$ transport is anomalous and super-diffusion is present.

Going back to our point vortex system, the motion of passive tracers is depicted in the Poincaré section depicted in Fig. 9. We can notice, that there are islands of regular motion, surrounded by a finite chaotic sea. When measuring transport, we shall consider only initial conditions in the stochastic sea, but since this chaotic region is bounded. Measuring plain dispersion is not convenient, it is however possible to circumvent this problem by working instead with length of trajectories and then to measure the dispersion of distance travelled among different trajectories.

$$s_i(t) = \int_0^t |v_i(\tau)| d\tau\,, \tag{52}$$

where $v_i(\tau)$ denotes the speed of particle i at time τ.

Once we have the length we can compute transport properties by computing the moments of the distribution

$$M_q(t) \equiv \langle |s(t) - \langle s(t) \rangle|^q \rangle\,, \tag{53}$$

where $\langle \ldots \rangle$ corresponds to ensemble averaging (average over different trajectories). Finally once we have the moments, we shall estimate the characteristic exponent of each moment, from its time evolution.

$$M_q(t) \sim t^{\mu(q)}\,. \tag{54}$$

As a result of this analysis the transport properties are found to be super-diffusive and multi-fractal [48], and this is the results of the memory effects engendered by stickiness. Stickiness is a phenomenon which is often found in Hamiltonian systems with mixed phase spaces, meaning phase spaces where regions of regular motion coexists with region of chaotic motion. When this is the case, in the vicinity of an island, trajectories can stay for for arbitrary large times, we can think of them

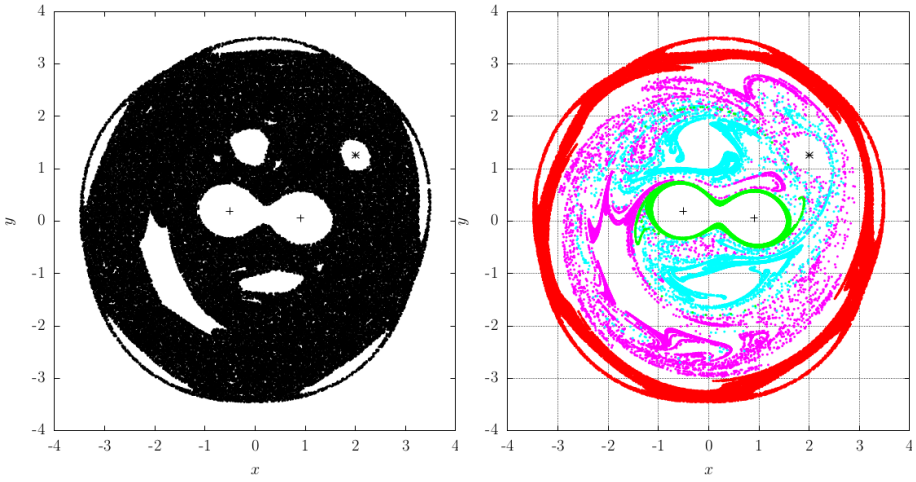

Fig. 9 Left: Poincaré section of passive particle in a flow generated by three point vortices. Right: localization of sticky regions contributing to different types of flights (see [48] for details).

mimicking the behavior of the regular trajectories nearby inside the island, these sticky borders act then as pseudo-traps [77, 78, 79, 80].

In the end, stickiness induces memory effects and implies a slow decay of correlations. This affects strongly transport properties and ends up in an anomalous super-diffusive transport.

In order to visualize the effect of stickiness, we have extracted from transport data the points which were corresponding to Lévy flights and then localized them on the Poincaré section. We can see clearly that sticky regions are responsible for these flights and are located near regular islands (note that not all islands are necessary sticky, see for instance[81]). The plot is drawn in Fig. 9 (see [48, 80] for details). To resume, once a trajectory sticks near an island, its length starts to grow almost linearly with time, it does so usually with an average speed generically different from the average peed over the chaotic sea. When looking at the transport data, this statement will imply the presence of of Lévy flights in. In Fig. 9, we can see that four different sticking regions are present. We can thus expect to have four different types of Lévy flights in our advected data.

4.2 Data processing

We shall now introduce the particularities of the data set from a signal processing point of view and describe the first step of the analyzing method.

A typical trajectory s is a one-dimensional signal of $N = 1000$ sampling points $s(t), t \in [1,N]$. An example of such signal is shown on Fig. 10 (left) and a set of trajectories on Fig. 10 (right). Several parts can be distinguished: a random fluctuation

(Brownian motion) and some *almost* linear segments of different length corresponding to Lévy flights.

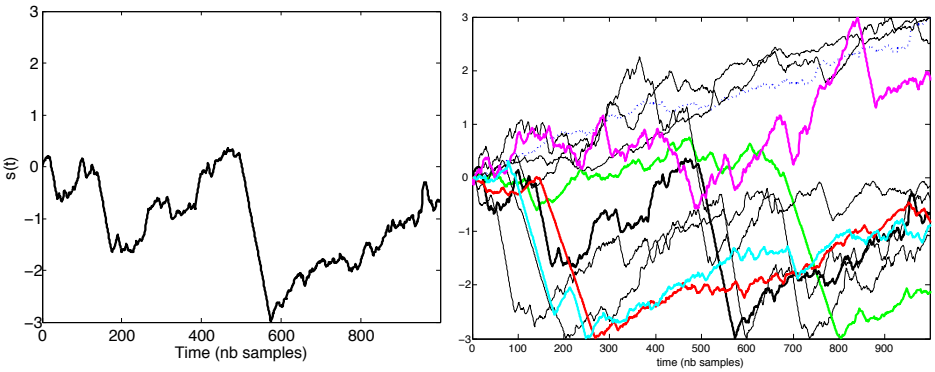

Fig. 10 Left: Arclength of the trajectory of a single particle, where several Lévy flights can be observed. Right: A set of trajectories of advected particles

4.2.1 A time frequency transformation

The robustness of our method relies on an uncertainty principle which is reminiscent of quantum mechanics. It can be shown that one can not measure exactly both frequency and time of a given signal. We use this latter relation to our advantage. Through an elementary transformation we turn random fluctuations of the signal amplitude into random fluctuations of the frequency of a new signal. When these frequencies are rapidly varying, as it is the case for random behaviors or noise in the signal, the uncertainty principle makes it impossible to have precise information on these variations. In the meantime, coherent behavior is emphasized since it is less fluctuating.

It is then important to notice that thanks to the uncertainty principle:

- random fluctuations in frequency cannot be rendered precisely in the time-frequency plane. It requires to be precise both in time and frequency, which is forbidden.
- linear parts or more generally slowly varying frequency components are emphasized by the time-frequency representation. Moreover, linear parts, called chirp signals, can be detected efficiently using the fractional Fourier transform.

It is then interesting and natural to take advantage of this fact for the analysis of the data set. To perform our analysis we shall therefore interpret the arclength $s(t)$ as the phase derivative (the fluctuation of the "frequency component") of a new signal $S(t)$. This corresponds to the first step of the process: Let us introduce the phase

$$\varphi(t) = \sum_{\tau=1}^{t} s(\tau), \tag{55}$$

and the signal

$$S(t) = e^{i\varphi(t)}. \tag{56}$$

The signal $S(t)$ is a non-stationary signal of magnitude one and made of a single frequency component which fluctuations are the one of the initial function $s(t)$.

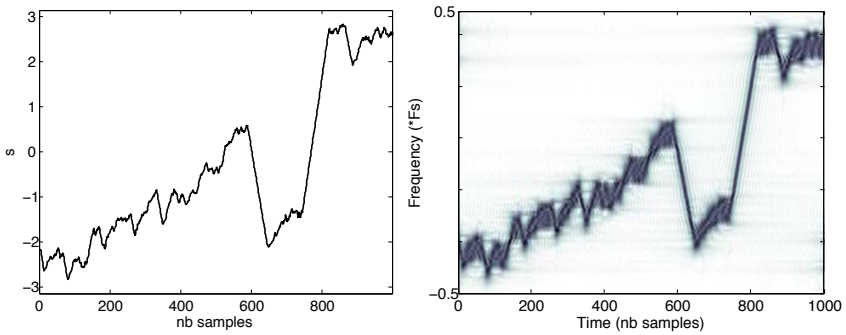

Fig. 11 Left: tracer trajectory s with fluctuating regions and linear regions (Lévy flights). Right: Gabor Transform (spectrogram) of S (absolute value of the short-time Fourier transform of S). Darker regions are associated to high values of $|\mathscr{V}_S|$.

The time-frequency representation (Gabor transform [6]) of S presented on Fig. 11 (right) is the absolute value of the short-time Fourier transform of S. One single frequency component can be seen which mimic the behavior of the signal s plotted on the left. But the important difference is now, because of the uncertainty principle, that brownian fluctuations become diffuse stains in Fig. 11 (right).

A consequence of this time frequency transformation is that the random behavior is blurred even more, spread over a neighborhood zone, whereas the linear parts remain relatively sharp.

Our first objective is attained: the linear behavior has been emphasized over the brownian motion, thanks to the uncertainty principle.

4.3 Tomographic analysis

For the detection of linear behavior in chaotic signals, we need a method able to detect these straight line patterns. In a 2 dimensional image, one would use techniques such as the Hough transform. In our case, we need a similar tool retrieving straight lines which would appear when a time-frequency decomposition is done (such as the short-time Fourier transform, the Gabor transform, or the Wigner-Ville transform). The appropriate tool for this purpose is based on the time-frequency tomogram.

In part 3.5 we describe in details the time-frequency tomogram applied to a reflectometry signal of finite duration T.

In this application, projections of the reflectometry signal an orthogonal basis $\left\{\Psi_{x_n}^{\theta,T}(t)\right\}_{x_0,\ldots,x_N}$ are used to extract the different components of the signal (see part 3.5.2). Each element of the basis $\Psi_{x_n}^{\theta,T}(t)$ is equal to :

$$\Psi_{x_n}^{\theta,T}(t) = \frac{1}{\sqrt{T}} e^{i\left(\frac{-\cos\theta}{2\sin\theta}t^2 + \frac{x_n}{\sin\theta}t\right)} = \frac{1}{\sqrt{T}} e^{i\alpha(t)}\,. \tag{57}$$

We can notice that the phase derivative $\frac{d\alpha}{dt}$ is linear :

$$\frac{d\alpha}{dt}(t) = -\frac{1}{\tan\theta}t + \frac{x_n}{\sin\theta}\,. \tag{58}$$

That means that the projections of a signal on such basis will be appropriate to detect linear part of its phase derivative. Considering a signal with a linear phase derivative such $s(t) = e^{i(\frac{b}{2}t^2+ct)}$, it is easy to demonstrate that the set of projections on an orthogonal basis :

$$c_{x_n,\theta}^{s} = < S, \Psi_{x_n}^{\theta,T} >\,, \tag{59}$$

is maximal for $\theta_M = \arctan(\frac{1}{b})$ and $x_M = c\sin\theta_m$.

The time-frequency tomogram will then be used to detect linear part in the phase derivative of the signal $S(t) = e^{i\varphi(t)}$ (Eq. 56), where the phase derivative is the arclength $s(t)$ of the particle (Eq.55).

In order to detect the different slopes of the Lévy flights it is necessary to apply the time-frequency tomogram for different θ_k regularly spaced and search the maxima in the projections c_{x_n,θ_k}^{S}.The number of selected θ_k is fixed by the user depending on how accurate he wants to be and is independent of the length of the signal N. The fast implementation of the time-frequency tomogram is of complexity $\mathcal{O}(N\log N)$, hence the overall complexity is of the same order.

The time-frequency tomogram can be reversed and it is possible to detect a linear part with slope $1/\tan\theta$ inside the signal then erase it in the (θ,μ) space and to re-synthesize the signal without this linear part by applying a time-frequency tomogram of angle $(-\theta)$.

4.4 Detection and characterization of Lévy flights

4.4.1 Method

On the signal shown in Fig. 11, one can see several Lévy flights (left) which have been turned into linear chirps in the frequency-time plane (right). For a specific angle θ_{M1}, the time-frequency tomogram defined (Eq. 59) will produce one sharp peak corresponding to the presence of a chirp as it is illustrated in Fig. 12 (left), where $|c_{\theta_{M1}}(x_n)|$ is plotted. For $x_{M1} \sim 830$, the sharp peak $|c_{\theta_{M1}}(x_{M1})|$ gives evidence that

there is a Lévy flight with a particular slope related to θ_{M1} and length related to amplitude of the peak. This search for maxima is the process that detects linear parts in the time-frequency plane.

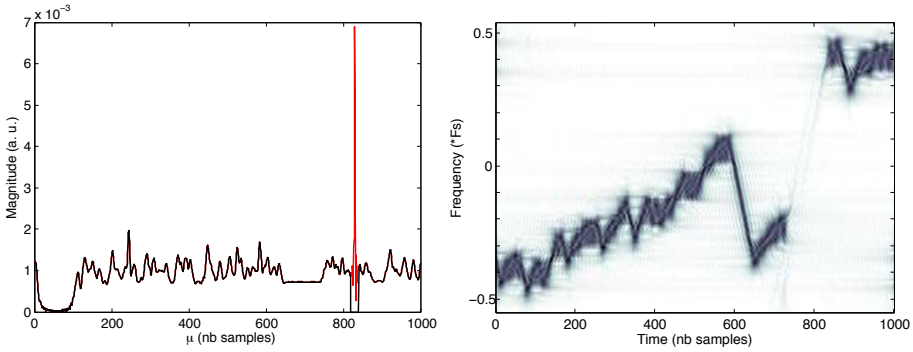

Fig. 12 Left: for θ_M, signal projections $|c_{\theta_M}(x_n)|$. Right : short-time Fourier transform of the signal S_1, partial reconstruction of S. The longest Lévy flight has been removed.

Since the time-frequency tomogram is invertible (see part 3.5.2), we can resynthesize the signal back to the initial representation after setting the values of the transform in red region of Fig. 12 (left) to zero. This result is illustrated on Fig. 12 (right), which represents the short-time Fourier transform of the newly recreated signal S_1. The largest frequency slope of S has been completely removed, the rest remaining untouched. This shows that indeed the peaks in the FRFT correspond to Lévy flights.

The method to detect linear parts of the phase derivative of the signal $S(t)$ is described by the following steps :

- compute the time-frequency tomogram of the signal $S(t)$, $|c^S_{\theta_k}(x_n)|$ for K values θ_k and N samples x_n:

$$c_{\theta_k}(x_n) = < S, \Psi^{\theta_k,T}_{x_n} > = \frac{1}{\sqrt{T}} \int_0^T S(t) e^{-i\left(\frac{-\cos\theta}{2\sin\theta} t^2 + \frac{x_n}{\sin\theta} t\right)} dt \,, \tag{60}$$

- extract the maximum from the $N \times K$ projections $|c^S_{\theta_k}(x_n)|$, θ_M, x_M will give the slope and the position of the first detection.
- reconstruction of the signal $S_1(t)$, where the linear part of the phase derivative is removed. A set $c^{S_1}_{\theta_M}(x_n)$ is obtained with the projections at the angle θ_M, where $|c^S_{\theta_M}(x_M)|$ and some coefficients of a small neighborhood are put to zero.

$$S_1(t) = \sum_{x_n} c^{S_1}_{\theta_M}(x_n) \Psi^{\theta_M,T}_{x_n}(t) \,, \tag{61}$$

- repeat the process with $S_1(t)$ for other detections.

When the signal $S_p(t) = e^{i\phi_P(t)}$ is obtained, after p detections of Lévy flights in the phase derivative, we will estimate the arclength of trajectory $s_p(t)$ where the Lévy flights are removed :

$$s_P(t) = -i\frac{\partial S_p(t)/\partial t}{S_p(t)}\,. \tag{62}$$

Then $s_p(t)$ will be compared to $s(t)$ and the Lévy flights will be characterized by their length in time, Δl and their velocity $v_s = \Delta h/\delta l$.

This process is applied to the tracer trajectory s plotted on Fig 11 (left). After two iterations, the linear part of the phase derivative of $S(t)$ are removed, as it can be see on Fig. 13 (left). The tracer trajectory $s_2(t)$ where the Lévy flights have been removed is compared to the original $s(t)$ on Fig. 13 (right). Then, the flights are characterized by their length and velocity.

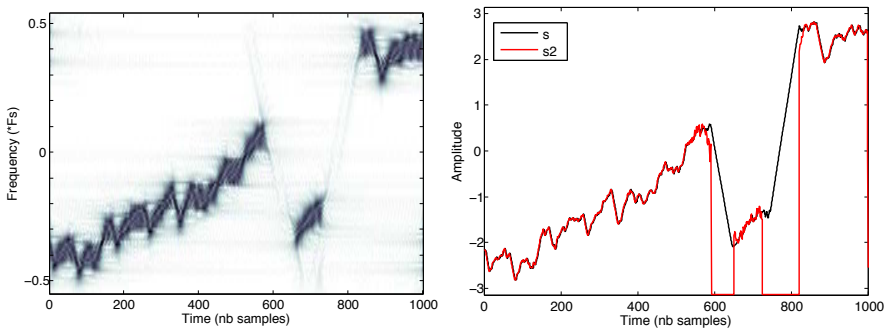

Fig. 13 Left: short-time Fourier transform of the signal S_2 where two Lévy flights have been removed. Right : original signal s (black) and partial reconstruction $s2$, without Lévy flights (red).

4.4.2 Results

We now consider blindly data obtained from the advection of 250 tracers in the point vector flow described in the previous subsection. That is to say, we analyze with our method 250 signals. We set up a threshold on the modulus of the projection coefficients in order to select only the most relevant Lévy flights. Similar transport data was analyzed in [48], with traditional tools and found to be anomalous and super diffusive. As mentioned, the starting point of the anomaly was traced back to a multi fractal nature of transport linked to stickiness on four different regular regions. One would thus expect four different types of Lévy flights in the data (see Fig. 9).

In the present case, the method described above has been applied to the data set. Our goal is to detect the multi-fractal nature of the transport resulting from the

sticky islands, which would serve as a proof of concept and pave the way to apply the method to numerical and experimental data. The results are presented in Fig. 14.

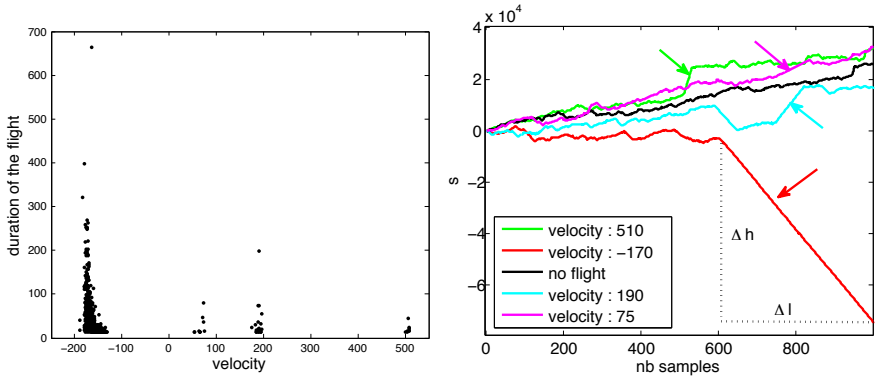

Fig. 14 Left: duration of the Lévy flights as a function of the velocity. Right: the velocity of the main Lévy flight is plotted for each trajectory.

For each trajectory, Lévy flights have been detected and characterized by their length in time, Δl, and velocity, $\Delta h/\Delta l = s$. The process described in detail above, gives, for each flight, its slope (related to the velocity) and length.

The Fig. 14 (left) is an illustration of the duration of the flights as a function of the velocity: four different values have been estimated ($\sim -170, \sim 75, \sim 190$ and ~ 510), which means that there are four different types of Lévy flights, as anticipated. We mention as well that for some trajectories no Lévy flights have been detected. A few few typical trajectories with Lévy flights have been plotted on Fig. 14 (right). The color coding corresponds to the one already used in Fig. 9, so that each specific detected flight can be easily associated to its originating sticky region. The agreement with the results found in [48], confirms that our method is successful, and is thus ready to be applied to various numerical and experimental data.

5 Perspectives

After a first time frequency transformation, where the signal s is transformed as the phase derivative of a new signal S, the time frequency tomogram is used to detect Lévy flights which are transformed as a linear phase derivative of S. This transformation makes use of the uncertainty principle : there is a "dilution effect" on the rapidly varying chaotic parts of the signal s while coherent patterns (Lévy flights) are only slightly affected. This part is critical for the robustness of the detection. Numerical simulations show that our technique is indeed extremely robust.

The time-frequency tomogram will give a sparse representation of the data of interest: Lévy flights become sharp peaks in the set of projections $c_{\theta k}(x_n)$. The key

point is that we knew the pattern we want to detect and chose the transformation in consequence.

The door is open to further extension and generalization of our method, providing that one knows *a priori* the patterns to detect which may not be linear but curved or some other slowly varying shape (slowly varying with respect of the chaotic fluctuations). A different representation from the tomogram should be used based on the shape information. One may use a basis or a set of vectors different from the set of linear chirps. Possible alternatives may be found in e.g.[8, 21] where what they call "tomograms" are bases of bended chirps and other more general time-frequency forms, associated to one or more parameters (equivalent of θ in the time-frequency tomogram case). One may also think of Gabor frames made of chirped windows[82]. Once the representation in which the relevant information is sparse has been found, the peak detection process remains the same.

6 Conclusion

This chapter is an attempt to show how non-commutative tomography can be used as an efficient and powerful signal processing tool. The approach is based on the physical analogies with the the non-commutative nature between time and frequency, and actually use this to our advantage in order to "clean" signals from undesirable noise. For such purposes we started this chapter with a slow step by step introduction of the mathematical notions behind non-commutative tomography. We tried to emphasize on some simple specific examples in order to give the non-mathematical reader some possible intuitions on the nature of the considered transforms.

From then on we considered data originating from magnetized fusion plasmas, namely reflectometry data of the plasma. We first briefly introduce the field of tokamak plasmas and then discussed the ideas behind reflectometry and how reflectometers work, as well as how data is acquired and processed. We then showed how using tomogram techniques allowed to clearly separate relevant data from unnecessary reflections on the tokamak walls or on the initial porthole. In this context, the fact that the original signal sent into the plasma is a chirp, meaning a signal whose frequency varies linearly in time allowed us to select a specific family reminiscent of fractional Fourier transform, which are particularly adapted for such signals. The actual experimental data was then analyzed and for some specific value of frequency-time mixture, we were able to clearly distinguish between the different reflection of the original signal. Hence using the reconstructing technique we were able to filter out on the fly the data, in order to recover only the useful reflection on the plasma which is useful for instance in order to reconstruct time dependent density profiles.

As a second application we considered data corresponding to the advection of so-called passive tracers in the flow generated by three point vortices. The dynamics of these tracers is Hamiltonian but due to the time dependent nature of the two dimensional flow, their trajectories are chaotic. Actually the phase space of passive tracers corresponds to the so-called mixed phase spaces, meaning that there are re-

gions where regular non-erratic motion is possible called regular islands, while there is a so called stochastic sea, where the motion is chaotic. In these mixed phase space the phenomenon of stickiness is able to generate long memory effects which affects transport properties, generating anomalous diffusion of tracers and the existence of long lasting Lévy flights. Using the analogy of considering a flight similar to the chirp signal used in the reflectometer, we performed a first simple transform of the signal in order to detect the chirp in the modified signal, which actually are flights in the original data. The method was shown to be successful in detecting the different Lévy flights present in the data, which were of different nature, as different sticking regions existed in the phase space.

In summary, we have showed in different contexts the efficiency of the signal processing method in two different cases, namely the case of reflectometry data and Lévy flights in advected data. Since in the context of magnetized fusion plasma there are some strong indications that transport is as well anomalous in the sense that it could be super-diffusive. It could be interesting to perform the Lévy analysis on reflectometer data, after the chirp flight trick has been performed. Should we detect as well some flights, it could be probably interesting to hard-code such signal processing treatment in a reflectometer to allow for fast plasma monitoring.

Acknowledgements Most of the works presented in this chapter are shared with our co-authors: Vladimir Man'ko, Margarita Man'ko, Rui Vilela Mendes, Ricardo Lima, Benjamin Ricaud, Frederic Clairet, Christine Bottereau. We woud like to take this opportunity to thank them and show our deep appreciation of our collaborations. We would like to thank as well Alberto Verga for a careful reading, and suggestions which improved the manuscript.

References

1. A.D. Poularikas (ed.), *The Transforms and Applications Handbook* (CRC Press & IEEE Press, 1996)
2. K.B. Wolf, *Integral Transforms in Science and Engineering* (Plenum Press, New York, 1979)
3. J.B.J. Fourier, *Théorie Analytique de la Chaleur*, *Oeuvres de Fourier*, vol. Tome premier (Gauthiers-Villars, 1888)
4. J.M. Combes, A. Grossmann, P. Tchamitchian (eds.), *Wavelets*. 2nd edition (Springer, 1990)
5. I. Daubechies, IEEE Trans. Inform. Theory **36**(5), 961 (1990)
6. C.K. Chui (ed.), *Wavelets: A Tutorial. Theory and Applications*, vol. 2 (Academic, 1992)
7. V.I. Man'ko, R. Vilela Mendes, Phys. Lett. A **263**, 53 (1999)
8. M.A. Man'ko, V.I. Man'ko, R. Vilela Mendes, J. Phys. A: Math. Gen. **34**, 8321 (2001)
9. S. Qian, D. Chen, *Joint time–frequency analysis* (Prentice-Hall, 1995)
10. J.B. Allen, L.R. Rabiner, Proc. IEEE **65**, 1558 (1977)
11. M.R. Portonoff, IEEE Trans. on Acoust., Speech and Signal Proc. **ASSP-28**(1), 55 (1980)
12. S.H. Nawwab, T.F. Quatieri, *Short-time Fourier Transform* (Prentice Hall, 1988), pp. 289–337
13. J. Morlet, **10**, 233 (1982)
14. B. Torresani, *Analyse continue par ondelettes* (InterEditions / CNRS Editions, 1995)
15. A. Grossmann, J. Morlet, SIAM J. Math. Anal. **15**, 723 (1984)
16. E. Wigner, Phys. Rev. **40**, 749 (1932)
17. J. Ville, Cables et Transmission **2**(A), 61 (1948)
18. L. Cohen, J. Math. Phys. **7**, 781 (1966)

19. L. Cohen, Proc. IEEE **77**, 941 (1989)
20. S.R. Deans, *The Radon Transform and Some of Its Applications* (John Wiley & Sons, 1983)
21. F. Briolle, V.I. Man'ko, B. Ricaud, R. Vilela Mendes, J. Russian Laser Res. **336**(2), 103 (2012)
22. I.M. Gelfand, M.I. Graev, N.Y. Vilenkin, *Generalized Functions, Integral Geometry and Representation Theory*, vol. vol.5 (Academic Press, New York, 1966)
23. J.C. Woods, D.T. Barry, IEEE Trans. Signal Process. **42**, 2105 (1994)
24. J. Wood, D.T. Barry, IEEE Trans. on Signal Process. **42**, 3166 (1994)
25. S. Barbarossa, IEEE Trans. on Signal Process. **43**, 1511 (1995)
26. S. De Nicola, R. Fedele, M.A. Manko, V.I. Man'ko, Theor. Math. Phys. **144**, 1206 (2005)
27. H.M. Ozaktas, Z. Zalevsky, M. Alper Kutay, *The Fractional Fourier Transform with Applications in optics and Signal Processing* (John Wiley and Sons Ltd, 2001)
28. F. Briolle, X. Leoncini, R. Ricaud, Discontinuity, Nonlinearity and Complexity **To be published** (2013). DOI 10.1109/NSC.2012.6304726
29. W. Horton, Rev. Mod. Phys. **71**, 735 (1999)
30. C. Laviron, A.J.H. Donne, M.E. Manso, J. Sanchez, Plasma Phys. Control. Fusion **38**, 905 (1999)
31. R. Nazikian, E. Mazzucato, Rev. Sci. Instrum. **66**, 392 (1995)
32. F. Briolle, R. Lima, V.I. Man'ko, R. Vilela Mendes, Meas. Sci. Technol. **20**(10), 105501 (2009)
33. F. Briolle, R. Lima, R. Vilela Mendes, Meas. Sci. Technol. **20**(10), 105502 (2009)
34. T.H. Stix, *The theory of plasma waves* (Mc-Graw-Hill, 1962)
35. J.M. Rax, *Physique des plasmas* (Dunod, 2006)
36. V.L. Ginzburg, *The Propagation of Electro-magnetic Waves in Plasmas* (Pergamon, 1964)
37. R.J. Colchin, ORNL Technical Memo **93** (1973)
38. Hartfuss H J, Geist T and Hirsh M 1997 Plasma Phys. Control. Fusion 39 1693
39. H. Bottollier-Curtet, G. Ichtchenko, Rev. Sci. Instrum. **58**(539) (1987)
40. F. Clairet, C. Bottereau, J.M. Chareau, M. Paume, R. Sabot, Plasma Phys. Control. Fusion **43**, 429 (2001)
41. F. Clairet, R. Sabot, R.C. Bottereau, J.M. Chareau, M. Paume, S. Heuraux, M. Colin, S. Hacquin, G. Leclert, Rev. Sci. Instrum. **72**, 340 (2001)
42. F. Clairet, C. Bottereau, J.M. Chareau, R. Sabot, Rev. Sci. Instrum. **74**, 1481 (2003)
43. F. Clairet, B. Ricaud, F. Briolle, S. Heuraux, C. Bottereau, Rev. Sci. Instrum. **82**(8) (2011)
44. C. Bottereau, F. Briolle, F. Clairet, J. Giacalone, M. Goniche, D. Molina, S. Poli, B. Ricaud, R. Sabot, (10th International Reflectometry Workshop, 2011)
45. *Traitement de données de réflectométrie pour la mise en évidence de phénomènes turbulents* (Conférences URSI "Propagation et Plasma", 2010)
46. *Tomogram analysis and reflectometry* (9nd International Workshop on Reflectometry, 2009)
47. X. Leoncini, in *Hamiltonian Chaos Beyond the KAM Theory*, ed. by A.C. Luo, V. Afraimovich, Nonlinear Physical Science (Springer, Berlin Heidelberg, 2011), pp. 143–192
48. X. Leoncini, L. Kuznetsov, G.M. Zaslavsky, Phys. Rev. E **63**(3), 036224 (2001)
49. X. Leoncini, O. Agullo, M. Muraglia, C. Chandre, Eur. Phys. J. B **53**(3), 351 (2006)
50. H. Aref, J. Fluid Mech. **143**, 1 (1984)
51. H. Aref, Phil. Trans. R. Soc. London A **333**, 273 (1990)
52. J. Ottino, Ann. Rev. Fluid Mech. **22**, 207 (1990)
53. J. Ottino., *The Kinematics of mixing: streching, chaos, and transport* (Cambridge U.P., Cambridge, 1989)
54. G.M. Zaslavsky, R.Z. Sagdeev, D.A. Usikov, A.A. Chernikov, *Weak Chaos and Quasiregular Patterns* (Cambridge Univ. Press,, Cambridge, 1991)
55. A. Crisanti, M. Falcioni, G. Paladin, A. Vulpiani, La Rivista del Nuovo Cimento **14**, 1 (1991)
56. T. Benzekri, C. Chandre, X. Leoncini, R. Lima, M. Vittot, Phys. Rev. Lett. **96**(12), 124503 (2006)
57. R. Bachelard, T. Benzekri, C. Chandre, X. Leoncini, M. Vittot, Phys. Rev. E **76**(4), 046217 (2007)
58. M. Brown, K. Smith, Phys. Fluids **3**, 1186 (1991)
59. R. Behringer, S. Meyers, H. Swinney, Phys. Fluids A **3**, 1243 (1991)

60. A.A. Chernikov, B.A. Petrovichev, A.V. Rogal'sky, R.Z. Sagdeev, G.M. Zaslavsky, Phys. Lett. A **144**, 127 (1990)
61. F. Dupont, R.I. McLachlan, V. Zeitlin, Phys. Fluids **10**(12), 3185 (1998)
62. A. Crisanti, M. Falcioni, A. Provenzale, P. Tanga, A. Vulpiani, Phys. Fluids A **4**, 1805 (1992)
63. B.A. Carreras, V.E. Lynch, L. Garcia, M. Edelman, G.M. Zaslavsky, Chaos **13**(4), 1175 (2003)
64. S.V. Annibaldi, G. Manfredi, R.O. Dendy, L.O. Drury, Plasma Phys. Control. Fusion **42**, L13 (2000)
65. D. del Castillo-Negrete, B.A. Carreras, V.E. Lynch, Phys. Plasmas **11**(8), 3584 (2004)
66. X. Leoncini, O. Agullo, S. Benkadda, G.M. Zaslavsky, Phys. Rev. E **72**(2), 026218 (2005)
67. C. Marchioro, M. Pulvirenti, *Mathematical theory of uncompressible nonviscous fluids*, *Applied mathematical science*, vol. 96 (Springer-Verlag, New York, 1994)
68. E.A. Novikov, Y.B. Sedov, Sov. Phys. JETP **48**, 440 (1978)
69. H. Aref, N. Pomphrey, Phys. Lett. A **78**, 297 (1980)
70. X. Leoncini, L. Kuznetsov, G.M. Zaslavsky, Phys. Fluids **12**, 1911 (2000)
71. X. Leoncini, G.M. Zaslavsky, Phys. Rev. E **65**(4), 046216 (2002)
72. X. Leoncini, A. Verga, Eur. Phys. J. B **86**(3), 95 (2013)
73. X. Leoncini, A. Barrat, C. Josserand, S. Villain-Guillot, Eur. Phys. J. B **82**, 173 (2011)
74. A. Laforgia, X. Leoncini, L. Kuznetsov, G.M. Zaslavsky, Eur. Phys. J. B **20**, 427 (2001)
75. L. Kuznetsov, G.M. Zaslavsky, Phys. Rev. E **58**, 7330 (1998)
76. L. Kuznetsov, G.M. Zaslavsky, Phys. Rev. E **61**, 3777 (2000)
77. G.M. Zaslavsky, Phys. Rep. **371**, 641 (2002)
78. X. Leoncini, L. Kuznetsov, G.M. Zaslavsky, Chaos, Solitons and Fractals **19**, 259 (2004)
79. X. Leoncini, C. Chandre, O. Ourrad, C. R. Mecanique **336**, 530 (2008)
80. B. Meziani, O. Ourrad, X. Leoncini, in *Chaos, Complexity and Transport* (World Scientific, 2012)
81. X. Leoncini, A. Neishtadt, A. Vasiliev, Phys. Rev. E **79**(2), 026213 (2009)
82. R.G. Baraniuk, D.L. Jones, IEEE Trans. Sig. Proc. **41**(12), 3543 (1993)